# Conjugate ionospheric perturbation during the 2017 solar eclipse

**Shun-Rong Zhang[1], Philip J. Erickson[1], Juha Vierinen[2], Ercha Aa[1], William Rideout[1], Anthea J. Coster[1] Larisa P. Goncharenko [1]**

[1]MIT Haystack Observatory
[2]University of Tromsø, Tromsø, Norway

**Key Points:**

- Persistent ionospheric density depletion in conjugate lower latitudes was identified during 21 August 2017 Solar Eclipse
- Conjugate depletion moved equatorward with eclipse progression and was coincident with weakening conjugate/southern equatorial ionization anomaly
- Plasma pressure reduction in flux tubes shadowed by the Moon, along with disturbed northward trans-equator winds, prohibits fountain plasma southward diffusion

Corresponding author: Shun-Rong Zhang, shunrong@mit.edu

## Abstract

We report new findings of total electron content (TEC) perturbations in the southern hemisphere at conjugate locations to the northern eclipse on 21 August 2017. We identified a persistent conjugate TEC depletion by 10-15% during the eclipse time, elongating along magnetic latitudes with at least ∼5° latitudinal width. As the Moon's shadow swept southward, this conjugate depletion moved northward and became most pronounced at lower magnetic latitudes (>-20°N). This depletion was coincident with a weakening of the southern crest of the equatorial ionization anomaly (EIA), while the northern EIA crest stayed almost undisturbed or was slightly enhanced. We suggest these conjugate perturbations were associated with dramatic eclipse initiated plasma pressure reductions in the flux tubes, with a large portion of shorter tubes located at low latitudes underneath the Moon's shadow. These short L-shell tubes intersect with the F region ionosphere at low and equatorial latitudes. The plasma pressure gradient was markedly skewed northward in the flux tubes at low and equatorial latitudes, as was the neutral pressure. These effects caused a general northward motion tendency for plasma within the flux tubes, and inhibited normal southward diffusion of equatorial fountain plasma into the southern EIA region. We also identified post-eclipse ionospheric disturbances likely associated with the global propagation of eclipse-induced traveling atmospheric disturbances in alignment with the Moon's shadow moving direction.



## Plain Language Summary

A solar eclipse casts a supersonic moving shadow on Earth's atmosphere and impacts the upper atmosphere by masking solar irradiation. For a given location, this results in local reduction and recovery of photo-ionization and photo-absorption within ∼2 hours. However, on a much larger scale, the moving, eclipse induced EUV screening lasting for multiple hours drives dynamical ionospheric variations. A global perspective on the eclipse induced ionospheric perturbation is now possible due primarily to the availability of total electron content (TEC) worldwide data from Global Navigation Satellite System (GNSS) receiver coverage. This paper reports new findings on total electron content perturbations in the southern hemisphere conjugate to the northern eclipse on 21 August 2017. While the moving Moon shadow was expected to yield traveling atmospheric disturbances, observational signatures of post-eclipse traveling ionospheric disturbances propagating into the southern hemisphere were identified. Significantly, a persistent TEC depletion zone conjugate to the eclipse region occurred, elongated along magnetic latitudes with ∼5° latitudinal width, moving equatorward and most pronounced at lower magnetic latitudes (∼ -20°N and equatorward). This depletion was coincident with a weakening southern equatorial ionization anomaly (EIA) while the northern EIA remained unaffected or was slightly enhanced. We suggest that both conjugate density depletion and disappearance of the southern EIA were associated with dramatic plasma pressure reduction in the magnetic field flux tubes, which are short in length at low latitudes and traverse the ionospheric F region when being shadowed by the Moon for a significant time. The plasma pressure gradient was skewed northward at low and equatorial latitudes, and neutral pressure gradients followed suit. Ultimately, these effects drove an overall northward motion of plasma in the flux tubes, inhibiting the normal southward diffusion of equatorial fountain plasma into the southern EIA region.


## 1 Introduction

A solar eclipse impacts the ionosphere due to a sudden reduction in solar irradiation (and therefore in photo-ionization and photo-absorption rates) as the Moon shadow sweeps through the Earth's atmosphere at a supersonic speed. This reduction results in ionospheric perturbations, both altitude and geophysical location dependent. Most eclipse induced local ionospheric perturbations have been explained by various coexisting pho-

tochemical and dynamic processes under the direct influence of solar irradiation reduction (Rishbeth, 1968), including ion production reduction, ionospheric and thermospheric cooling (thermal contraction), ambipolar plasma diffusion and topside ion flow (MacPherson et al., 2000; Yau et al., 2018; Hairston et al., 2018; Goncharenko et al., 2018), as well as disturbances in neutral winds, composition (Harding et al., 2018; Wang et al., 2019; Lei et al., 2018; Wu et al., 2018; Müller-Wodarg et al., 1998), and electric field perturbations (Maurice et al., 2011; Huba & Drob, 2017; Dang, Lei, Wang, Burns, et al., 2018; Chen et al., 2019). By contrast, regional eclipse induced variations have become better known only recently with the wide availability of ionospheric measurements, especially total electron content (TEC) from GNSS receiver networks (A. J. Coster et al., 2017; He et al., 2018; Cherniak & Zakharenkova, 2018). Examples of particularly notable regional effects include bow-shaped ionospheric waves (Zhang et al., 2017; Liu et al., 2011) and other atmospheric wave induced fluctuations (Sun et al., 2018; Nayak & Yiğit, 2018; Perry et al., 2019; Eisenbeis et al., 2019), ionospheric features arising from radiation inhomogeneity on the solar disk (Mrak et al., 2018), and the polar region impact (Dang, Lei, Wang, Burns, et al., 2018). Global scale eclipse effects, however, have to date been largely based on theoretical estimates and need to be validated with solid observational evidence.

Two important aspects are relevant for eclipse global effects and in particular conjugate hemispheric effects. The first aspect is associated with excitation of large scale traveling atmospheric disturbances (TADs) and their subsequent global propagation. TADs can be launched due to sudden cooling that is sweeping rapidly through the upper atmosphere. Key effects here are neutral temperature reduction, spatial homogeneity of pressure gradient, and wind convergence (Lei et al., 2018; Dang, Lei, Wang, Zhang, et al., 2018; Lin et al., 2018; Cnossen et al., 2019; Wu et al., 2018; Harding et al., 2018; Wang et al., 2019; Müller-Wodarg et al., 1998). TADs travel globally even across the equator, depending on the exact eclipse path and, particularly, the history of that path due to the changing direction of the associated atmospheric pressure gradient. Many of these simulations indicate that post-eclipse TADs are essentially a continuation of the global propagation of the eclipse-induced TADs. While neutral wind observations have confirmed this post-eclipse TAD effect (Harding et al., 2018), substantial evidence for the post-eclipse TIDs has not been well established, although highly anticipated due to the close TAD/TID relationship. The second aspect is a remote effect occurring at eclipse conjugate locations. At mid- and low latitudes, magnetic field lines provide strong electrodynamic coupling that connects the ionospheres underneath the Moon shadow and in the conjugate hemisphere through several hypothesized processes. Possibilities include:

(1) Photoelectron flux from the sunlit ionosphere loads into the conjugate eclipse hemisphere, where the ionosphere is cooled down and collapses very much like an accelerated version of a sunset. The impact of photoelectrons from the conjugate sunlit ionosphere on the hemisphere in darkness has been observed and well explained in earlier work (Carlson Jr., 1966; Evans & Gastman, 1970). During an eclipse, these conjugate photoelectrons can compensate for primary, local EUV reduction, and this effect becomes increasingly significant with altitude due to photoelectron loss in the eclipsed (local) ionosphere from photo-ionization reduction (MacPherson et al., 2000). This compensation process could potentially provide a causal connection that would explain a weaker electron temperature ($T_e$) reduction shown in the August 2017 eclipse Goncharenko et al. (2018) compared to model simulations by Cnossen et al. (2019) where conjugate photoelectron effects were not included. However, separate modeling by Le et al. (2009); Huba and Drob (2017) demonstrated electron cooling in the entire flux tube that thermally connects both hemispheres through rapid field-aligned thermal conduction. Such conjugate hemisphere cooling can potentially alter thermodynamics and eventually electron density ($N_e$) by several processes. However, due to the strong dependence of $T_e$ on $N_e$, excessive $N_e$ reduction (increase) normally tends to increase (decrease) $T_e$, with this trend depending significantly on the absence of external energy input. For these reasons, it is

therefore important to examine $T_e$ and $N_e$ simultaneously to understand $T_e$ ionospheric variations.

(2) Electric fields are induced by the eclipse due to ionospheric dynamo modification by substantial conductivity and/or neutral wind changes in the E and F regions. These effects can be mapped into the conjugate ionosphere as long as conjugate current short-circuiting in the E region is not present (Huba & Drob, 2017; Dang, Lei, Wang, Burns, et al., 2018). If the eclipse falls into magnetic low and equatorial latitudes, such additional electric fields could potentially modify the regular equatorial ionization anomaly (EIA) (Maurice et al., 2011; Chen et al., 2019).

The 21 August 2017 solar eclipse presented an unprecedented modern observational opportunity to examine some of these hypotheses on conjugate ionospheric variations, thanks to the excellent available spatial coverage of GNSS TEC observations over the continental US (CONUS) as well as reasonable coverage in South America. Previous attempts (He et al., 2018; Chen et al., 2019) have been able to hint at eclipse-induced conjugate changes, for example, He et al. (2018) showed the southern hemispheric TEC depletion from several GNSS individual receivers. But explicit substantial evidence, especially the spatial context with the eclipse in the northern hemisphere, was still not possible in those studies. In this work, we will provide GNSS TEC-based observational evidence of ionospheric eclipse time disturbances occurring in the conjugate ionosphere, and will characterize these disturbances in the context of the solar eclipse induced ionospheric dynamics. We conclude with two main findings: (1) Electron density ($N_e$) was depleted over eclipse conjugate ionospheric locations, coincident with weakening of the conjugate EIA; and (2) substantial large scale TIDs occurred, propagating southward and arriving at the conjugate hemisphere during the post-eclipse time period.

## 2 Method: Solar eclipse mapped to the conjugate ionosphere and GNSS TEC analysis technique

The 2017 Great America Solar Eclipse on 21 August, optically visible in the CONUS, started with a partial eclipse at 1604 UT (First Contact, $C_1$) over Oregon and traversed southeastward across the central part of CONUS, arriving at (-90°E, 36.5°N) at 18:20 UT (12:20 SLT) when totality occurred. The totality ended at 20:02 UT (Fourth Contact, $C_4$) near (-27°E, 11°N) and the partial eclipse ended at 21:04 UT ($P_4$) near the geographic equator. Of particular note, the eclipse progression toward southeast is an essential fact for our study as it determines to a large degree the TAD/TID propagation direction and the the conjugate ionospheric response pattern. Figure 1 shows the totality path over CONUS and its conjugate locations over the South America, as well as the Moon shadow area at the 300 km ionospheric height and the region of 25% solar obscuration magnitude at 19:00 UT in the northern hemisphere and its corresponding conjugate locations in the southern hemisphere. The obscuration magnitude (ratio) is calculated based on the fraction of the visible solar disk area screened by the Moon. The magnetic latitude mapping for conjugate latitudes is performed using Altitude Adjustment Corrected GeoMagnetic (AACGM) coordinates (Shepherd, 2014) at 300 km altitude. This 300 km was used to represent the conjugacy of the ionosphere at the F region height, and is close to the assumed 350 km altitude of the GNSS TEC ionospheric pierce point used for GNSS TEC data processing. This small altitude difference will have no visible effects on our eclipse effect analysis. The totality path spanned a range of mid- and low magnetic latitudes, and was ideally suited for examining latitude dependence of potential conjugate ionospheric variations. The best availability of GNSS TEC data in the conjugate South America ionosphere, as shown in the map, started at 19:00 UT (approximately in the early afternoon).

We analyzed ionospheric TEC data obtained around 21 August 2017. The GNSS processing algorithms that were used to produce TEC were developed at MIT Haystack

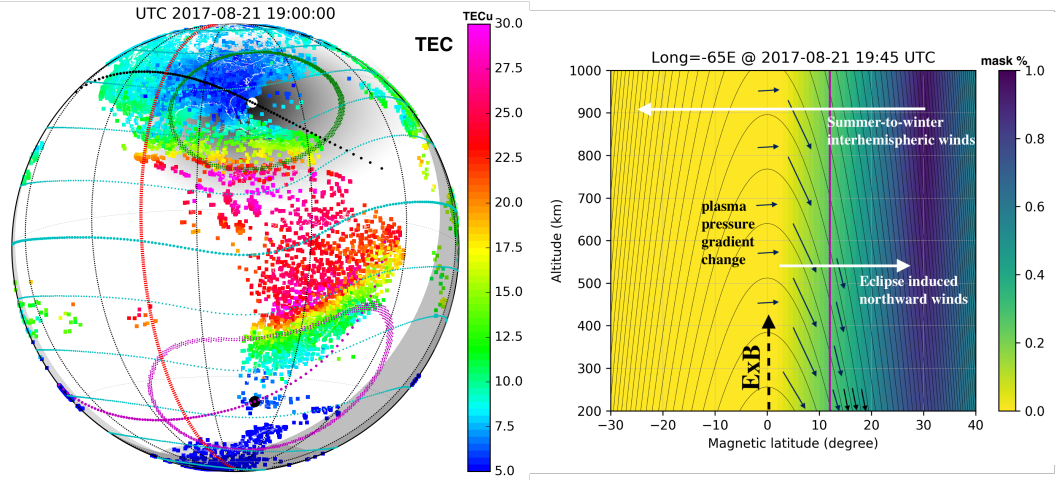


Figure 1: The 21 August 2017 solar eclipse as viewed globally. (left) The totality path (black dotted line) and the corresponding conjugate locations (magenta dotted line) are shown for the entire eclipse period. Shown also are the eclipse magnitude (calculated based on the fraction of the visible solar disk area screened by the Moon) for 19:00 UT represented by the shaded darkness, the 300-km eclipse magnitude contour at ∼25% (green dotted curve) and the corresponding conjugate locations (magenta dotted curve), as well as the approximate totality location (white dot) and its conjugate point (black dot) at this time. Magnetic latitude contours are provided at a 15° interval (cyan dotted curve) with magnetic equator marked as heavier cyan dotted curve. Local noon (on the ground) is the red line. GNSS TEC data with minimum elevation of line-of-sight 25° is provided for this time. Solar terminator (on the ground) and the nightside are also marked as the shaded area near the right side of the map. (right) Latitudinal and altitudinal variations at the -65°E cut in the eclipse magnitude (shaded) and L-shell curves. The 25% eclipse magnitude is marked as magenta lines. The schematic representation of the direction of plasma pressure gradient changes in the flux tubes underneath the Moon shadow is also provided as solid arrows. The E×B plasma drift that drives the plasma fountain at the magnetic equator is shown as a dashed arrow. The directions of neutral pressure gradient change and trans-equatorial winds are white arrows. The length of the arrows is not proportional and does not carry physical meaning.

Observatory (Rideout & Coster, 2006; Vierinen et al., 2016). This is the same data source used previously in Zhang et al. (2017); A. J. Coster et al. (2017), except that here a large amount of GLONASS data, in addition to GPS data, was added to increase coverage in South America. Overall, the newly added GLONASS data increased the amount of data by ∼30% over the nominal (baseline) 6000+ global receivers used for standard processing.

In order to detect ionospheric responses associated with the solar eclipse, we calculated differential TEC using an approach that effectively removes the background ionospheric "trend", as demonstrated in previous TID studies (Zhang et al., 2017; Zhang, Coster, et al., 2019; Zhang, Erickson, et al., 2019; Lyons et al., 2019; Sheng et al., 2020). Zhang, Coster, et al. (2019) provided more detailed discussions of this method. The essential approach is to work with individual receiver-satellite TEC data segments, and to subtract a background TEC variation determined by a low-pass filtering procedure using the Savitzky-Golay low-pass filter (Savitzky & Golay, 1964). The filter, implemented with a linear basis function, is similar to the procedure of calculating averages over sliding windows, where the size of the window (in time) can be conventionally controlled in

order to maintain different levels of smoothness in the background TEC. This approach allows study of fluctuations with different characteristics.

Differential TEC calculation of this nature is widely used for GNSS TEC based large and medium scale TID and ionospheric disturbance studies Saito et al. (1998); Tsugawa et al. (2007); Ding et al. (2007); Azeem et al. (2015); Chou et al. (2018); Astafyeva (2019). As our goal here is to examine large scale ionospheric perturbations associated with the eclipse and at a given location, the eclipse duration is normally contained within 2 hours, we primarily used a 2-hour sliding window for the differential TEC calculations. We also examined 1 hour window results for comparison. To be completely free from impacts of the data edge associated with the use of fixed length windows, we removed data for the first and the last 1-hour (0.5-hour) of each data segment when a 2-hour (1-hour) sliding window was used. This has the caveat that the 2-hour sliding window results in doubling the loss of data when compared with the 1-hour sliding window. Finally, our analysis disregarded the portion of data segment with satellite elevation $< 25°$. Final accuracy of this method derives from the accuracy of the GNSS phase measurement. Assuming that there is no loss of phase lock in the receiver, the error in differential TEC is less than 0.03 TEC units (A. Coster et al., 2012), as all satellite and receiver bias terms cancel out in a differential sense.

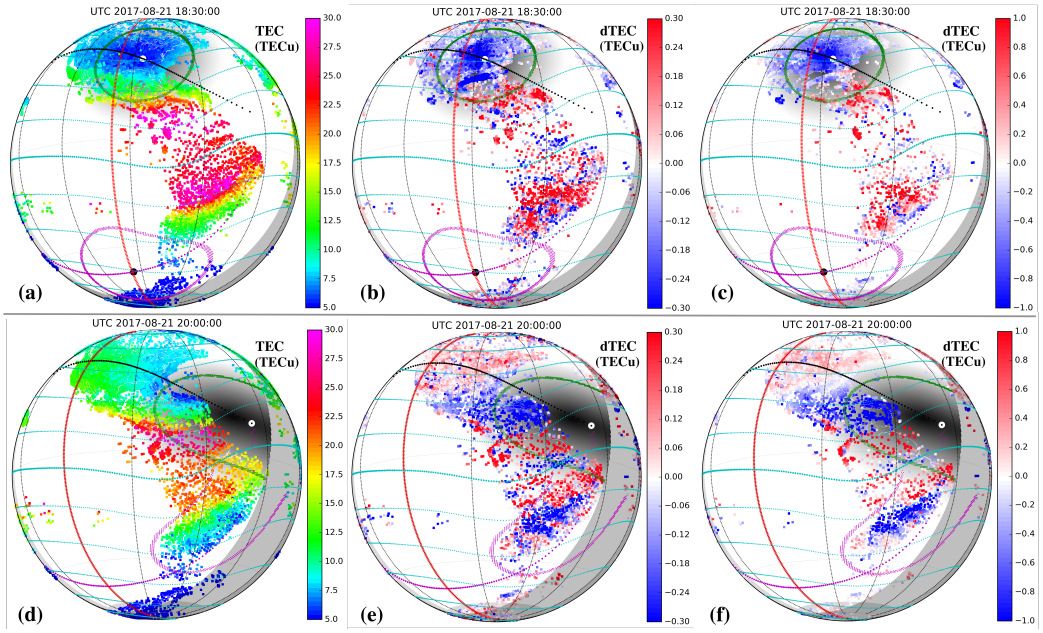


Figure 2: Detecting ionospheric changes during the presence of solar eclipse. Two groups, (a)-(c) as well as (d)-(f), of global maps are shown for 18:30 UT and 20:00 UT respectively at different stages of the eclipse. GNSS TEC maps are in (a) and (d), differential TEC (dTEC) maps after de-trending background variations using the low-pass filter with 60-min sliding windows are in (b) and (e), and with 120-min sliding windows in (c) and (f). Notice the different color scales for dTEC results with different sliding window filters. Similar eclipse and other information as in Figure 1 is also provided.

To examine the validity of this de-trending method, Figure 2 plots the original TEC and differential TEC calculated with 1-hour and 2-hour window sizes at two instances. Within the eclipse zone in the northern hemisphere, the differential TEC from both windows shows that TEC reduction was largest near totality but lagged behind it, consistent morphologically with results from TEC deviation relative to a reference, e.g., A. J. Coster

et al. (2017); Cherniak and Zakharenkova (2018). We emphasize that examining the deviation from a reference day would be inappropriate for the present study due to concerns arising from substantial day-to-day and other variability at low latitudes. Specifically, the 20 August was geomagnetically quiet and 22 August was more active, so 20 August could have been used as a reasonable reference. However, there was a significant morphology change at low and equatorial latitudes between 20 and 21 August, with EIAs on the eclipse day and without EIAs on the 20th (see Supplement figure S2). TEC differences between the two days would therefore reflect, to a large degree, the dominating EIA physics but would potentially wash out or distort variations with small amplitudes.

Owing to the nature of the de-trending technique, for a disturbance signature of 2 TECu peak-to-valley change, a 1 TECu deviation from the background trend will be identified in our procedure. Although the selection of the window length between 1 hour or 2 hours is somewhat arbitrary, the large-scale feature of the depletion shown in the 2-hour window was consistent with that in the 1-hour window despite an expectation of smaller amplitudes and fine structures in the 1-hour data. More generally, coherent depletion features in the conjugate hemisphere of the eclipse were very pronounced in both 1-hour and 2-hour differential TEC data, as well as in the original TEC data, and these features will be further discussed in the next section. A weaker depletion at equatorial latitudes was also found consistently from both data analysis methods, further suggesting a small reduction in the EIA plasma source region.

## 3 Conjugate ionospheric density depletions

### 3.1 General features

We first examined ionospheric perturbations from individual global maps of differential TEC (dTEC) during the eclipse period. Figure 3 plots dTEC from 19:15 - 21:00 UT on a 15 min cadence (except for 20:00 UT, contained in Figure 2(f)). The dTEC depletion area in the southern hemisphere was not identifiable until ∼19:00 UT (see 18:30 UT in Figure 2(c) and 19:15 UT in Figure 3(a)). At that time, low density developed near the northeast leading edge of the area conjugate to the 0.25 (25%) eclipse iso-magnitude curve (hereafter referred as " 0.25-curve"), and thereafter became well organized within the conjugate 0.25-curve. The depletion was observed predominantly near the equatorward side of the 0.25-curve (the poleward side had no data). The depletion structure partially visible with available data was elongated along the magnetic latitude with at least a ∼5° latitudinal span and a northern edge at ∼ -15°N and higher magnetic latitudes. As the Moon shadow moved southeastward in the northern hemisphere and the conjugate 0.25-curve moved northeastward accordingly, the depletion was extended further northeastward toward the magnetic equator and the terminator. After 20:15 UT, a period when only a partial eclipse was visible in the northern hemisphere and when the conjugate 0.25-curve was significantly smaller in coverage area, the eclipse-induced depletion became narrower in the meridional direction with its equatorward edge at ∼ -15°N magnetic latitude. However, this depletion feature survived even in the *wake of TIDs* (to be discussed later) which almost masked the depletion at ∼ 21:00 UT, and by 22:00 UT we note that it was still identifiable.

Post-eclipse (after 22:00 UT) ionospheric variations also exhibited obvious disturbances in the southern hemisphere. Figure 4 are dTEC maps between 22:00–00:30 UT. By 23:00 UT, the aforementioned depletion at low latitudes in the southern hemisphere has gradually faded away near -15°N magnetic latitudes. At 23:00 and 23:30 UT, negative dTEC was found in the latitudes where the eclipse was terminated (i.e., ∼15°N magnetic latitudes between -60 – -30°E in Figure 4(c)), to the immediate south of these latitudes (near the magnetic equator, Figure 4(c)), and further south (∼ -15°N magnetic latitude) in the conjugate hemisphere. This post-eclipse depletion in the eastern longi-

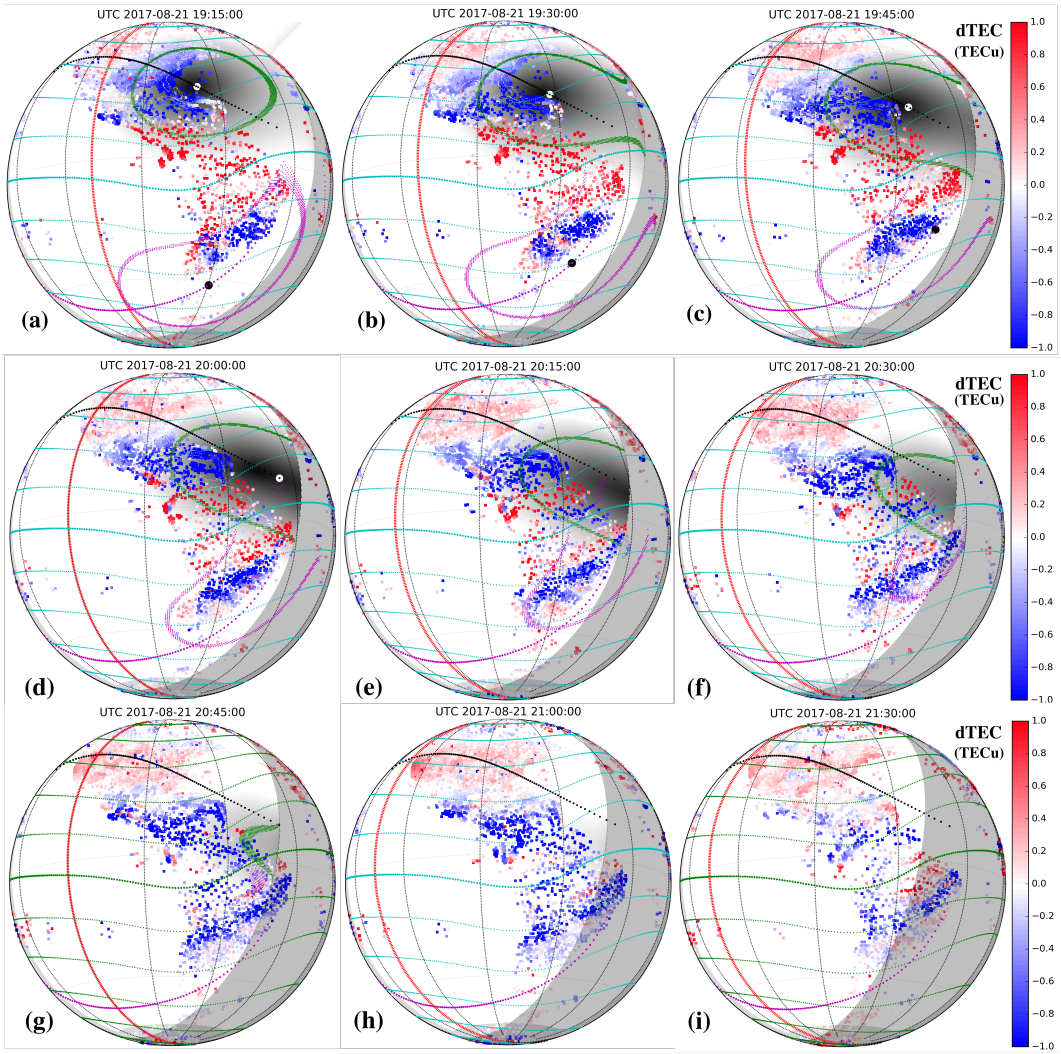


Figure 3: Global dTEC maps derived using the 120-min sliding window de-trending from 19:15 - 21:00 UT at a 15-min interval and at 21:30 UT.

tudes (∼ -60 – -30°E, Figure 4(d)) was then extended to the west (∼ -60°E and westward, Figures 4(e) and 4(f)) at later times. In these western longitudes, the distance to the northern eclipse zone is longer than that in the eastern longitudes and therefore the southward propagating thermospheric/ionospheric disturbances took a longer lag time to arrive. The negative dTEC zone was also found as south as -30°N magnetic latitude, with reduced amplitudes of dTEC.

### 3.2 Longitudinal and latitudinal variations

Next, we characterized the depletion evolution with time and latitude/longitude using keograms. The longitude - UT variation in dTEC at 4 geomagnetic latitude bands in the southern hemisphere is given in Figure 5 where the corresponding 0.25-curve (green dots) is used to guide identification of the eclipse influence. Latitudinal variations at -70 – -60°E and -60 – -40°E longitudes are presented as dTEC in percentage (relative to the background TEC) in Figure 6. Two distinct features which were essentially very consistent in the longitude range between -75 – -35°E are noted:

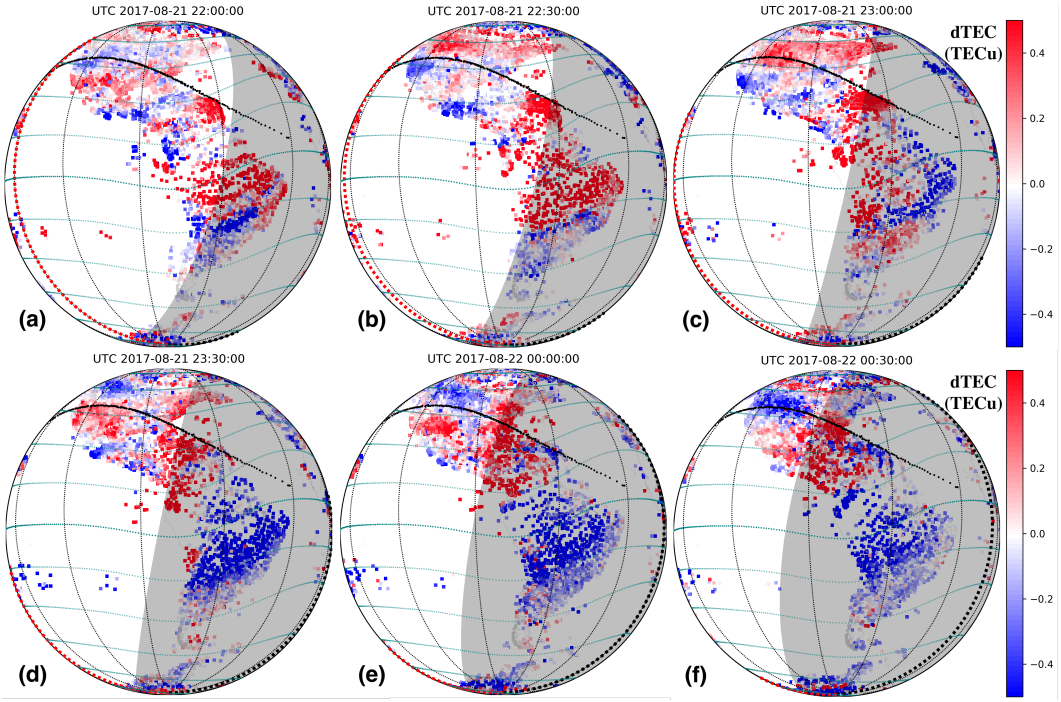


Figure 4: Same as Figure 3 but for the post-eclipse period between 22:00-00:30 UT with a 30 min interval. Notice the color scale changes from Figure 4.

(1) **Post-eclipse southward-propagating disturbance fronts**, shown in the depletion zone, change with latitude and time in Figure 5 panels (a)-(d). Specifically, the most pronounced depletion with negative dTEC appeared near but before 24 UT of 21 August at ∼ -10°N [in (a)] and similarly at ∼ -15°N latitudes [in (b)], then predominately at or immediately after 24 UT at a higher latitude ∼ -25°N [in (c-d)]. The amplitudes of these dTEC absolute values decreased southward as the disturbance propagated away from the northern eclipse region into the region of lower TEC background in the south. The positive dTEC disturbance fronts (areas between the two solid lines) arrived earlier, between 22-23 UT at ∼ -10°N and at 23 UT at ∼ -25°N. Note that the propagation of these disturbance fronts as shown in the keograms did not appear to be consistently correlated with the sunset terminator, and therefore we did not identify them as a sunset effect. Further ahead of (prior to) these positive dTEC fronts, clear indications of negative dTEC zones existed. However, these zones were much more complicated, resulting from the spatially overlapping between these disturbance fronts and the aforementioned northeast extension/progression of the conjugate density depletion (the green arrow line). The latitudinal variation of percentage dTEC in Figure 6 indicates that the dTEC negative zone initially in the northern hemisphere eclipse zone moved southward along with the eclipse shadow, and continued propagating beyond where the eclipse was terminated into the southern hemisphere. At 23:00 UT, the negative zone reached at least -40°N geographic latitude (see the left dark arrow); a positive disturbance front occurred at a later time (see the right dark arrow), and finally a negative disturbance front by ∼24:00 UT.

Figures 5 and 6 both indicate enhancement zones prior to the northern eclipse onset, which was after 18:00 UT at low latitudes for ∼ -70°E longitudes. These structures were clearly northward TIDs at low latitudes in both hemispheres (Figure 6), which had started in the southern hemisphere at ∼ 16:00 UT, well before the eclipse onset at those

longitudes. These TID features were consistent with Figures 7 and 8 which will be discussed next. Therefore, on top of these northward-propagating TIDs, the eclipse induced TEC depletion originally in the northern hemisphere propagated through in the opposite direction, and clearly modified the amplitudes of these regional TIDs.

(2) **An negative dTEC structure in the conjugate hemisphere** was evident inside the conjugate 0.25-curve, particularly in Figure 5 at $\sim$ -25°N and $\sim$ -20°N magnetic latitude bands, but was less evident northward into lower latitudes at $\sim$ -15°N and $\sim$ -10°N magnetic latitude bands (see the green arrow line). The negative dTEC was largest at $\sim$ -20°N but did not reach $\sim$ -10°N. Figure 6 further reveals that in general, the conjugate depletion zone moved northward toward the magnetic equator as the northern eclipse mask swept southward. At the eastern longitudes (-60 – -40°E) where the eclipse zone and its conjugate zone are closer to the magnetic equator, the location of the conjugate depletion zone was more at the center of the 0.25-curve than that for the western longitudes.

These two distinct features can be represented by a smoothed version of observations that are shown in Figures 5 and 6. This version is given in Figure 7 where running averages within 7.5 min and 10° latitude are calculated. This shows clearly the southward propagating disturbance (the green arrow) in the north hemisphere under the direct influences of the Moon mask, the post-eclipse southward propagation disturbance in the conjugate hemisphere (the gray arrow), and the northward progression of negative dTEC (the red arrow) in the conjugate hemisphere during the northern eclipse.

Finally, we used latitude-UT keograms to further delineate and summarize latitudinal variations of characteristic eclipse induced TIDs and conjugate TEC depletion in the longitude sector -75 – -60°E (Figure 8). Note here differential TEC is shown in percentage, and is in magnetic latitude. Results show dTEC variations by up to 10% relative to the smoothed (2-hour average) background trend, corresponding to roughly 20% deviation from the onset of eclipse effect. Region (1) was located underneath the Moon shadow as indicated by the 0.25-curve. The dTEC calculation effectively reveals direct eclipse influences and their latitudinal progression. Note that in these observations the slope of the depletion as a function of latitude and UT was initially larger: the green dashed line on the left (tracing the depletion inside the 0.25-curve) has an estimated slope of $\sim$ 650 m/s; the slope became slightly smaller toward the end of the eclipse before 21:00 UT. This changing slope is likely related to the latitudinal dependence of the eclipse penumbra moving speed. Region (2) was in latitudes with less than 25% eclipse obscuration as well as beyond the immediate end of the eclipse path at 21:04 UT (P4) when the eclipse was just terminated. The continuous extension of TEC depletion between 21-22 UT, beyond the eclipse termination, was identified as the initial sign of the post-eclipse TID. For a few hours (4-5 hours) since the eclipse termination, post-eclipse perturbations continued to be present in Region (3) that extended deep in the southern hemisphere. In Region (3) there was also a positive disturbance front. It appears reasonable to attribute these post-eclipse ionospheric disturbances in dTEC to large scale TIDs that were driven by post-eclipse TADs. As discussed in Introduction, TADs excited in situ in the thermosphere by a solar eclipse have been well-known in simulations. Their global propagation in the direction associated with the eclipse path will continue after the eclipse has terminated, and then become attenuated (Müller-Wodarg et al., 1998; Lei et al., 2018; Dang, Lei, Wang, Zhang, et al., 2018). These TADs are expected to drive TIDs through effects of the disturbance winds, temperature, and composition, and therefore post-eclipse TIDs are quite likely; in fact, Lei et al. (2018); Dang, Lei, Wang, Zhang, et al. (2018) were able to demonstrate the simulated post-eclipse electron density disturbances (positive and negative) in the southern hemisphere. Our post-eclipse dTEC observations were consistent with the southward propagation of the post-eclipse TADs through the southern hemisphere in some of these simulations.

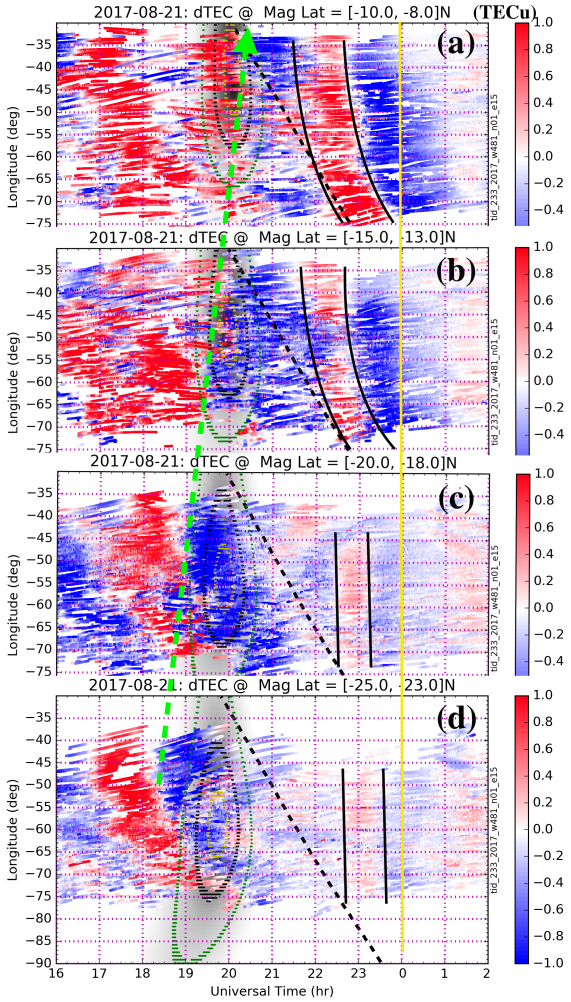


Figure 5: Longitudinal disturbances in dTEC (TECu) as a function of UT at magnetic southern latitudes (a) -8 – -10°N, (b) -13 – -15°N, (c) -18 – -20°N, and (d) -23 – -25°N. Green dots are conjugate locations of the 25% magnitude of eclipse in the northern hemisphere, and black dots are the same as the green except for the 50% magnitude. Dashed line represents the sunset times. Solid black lines mark the regions between positive and negative wave fronts of post-eclipse TIDs near 22–24 UT. Dashed green line highlights the equatorward progression of the depletion region. Yellow vertical line is 24 UT.

Region (4) is the TEC depletion (negative dTEC) zone in the southern hemisphere which remained within the conjugate 0.25-curve. It corresponds roughly to the southern depletion in Figure 3. The depletion initially developed near -40°N magnetic latitudes near 19 UT when the eclipse totality occurred in the north, and the depletion intensified at later times when the Moon shadow moved to lower latitudes. By 21 UT, the eclipse had terminated, post-eclipse TIDs became highly visible in Region (3), and the conjugate depletion zone remained in Region (4). Therefore these TIDs and the conjugate depletion partially overlapped.

To summarize these observational results, the eclipse induced ionospheric effect in the southern hemisphere was characterized by a TEC depletion zone located predominantly in a **triangle region** on the magnetic latitude - UT keogram as shown in Fig-

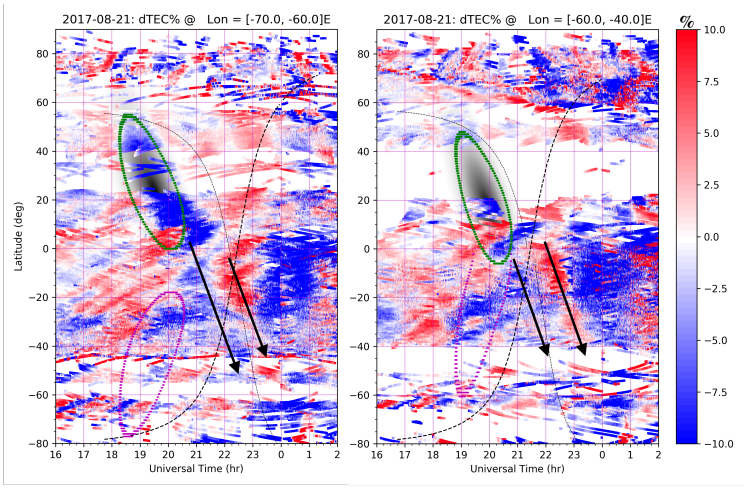


Figure 6: UT vs latitude variations of dTEC (in percentage) derived using the 120-min sliding window de-trending for longitudinal sectors (left) -70 – -60°E and (right) -60 – -40°E. The 0.25 eclipse magnitude is marked by the green line and its conjugate location is marked by the purple line. The dark arrows represent the eclipse-induced ionospheric disturbance propagation. Thick dashed line represents the sunset times, and the thin dashed line is the sunset times for corresponding conjugate locations.

ure 8. During the presence of the northern eclipse, the conjugate ionosphere experienced the density depletion that developed into lower latitudes at later times. Furthermore, during the post-eclipse period, both this conjugate ionospheric depletion and large scale TID influences were concurrent in both space (especially at lower latitudes) and time.

### 3.3 Southern EIA crest weakening

The largest depletion of conjugate ionospheric density disturbance (negative dTEC) during the northern eclipse was observed in the aforementioned triangle area at ∼30°S geographic latitude (∼ -20°N geomagnetic latitude) and equatorward as shown in Figures 6, 7 and 8, with a particularly large effect immediately adjacent to the southern EIA zone. The EIA crests in TEC were nearly symmetric in their location and intensity with respect to the magnetic equator before the eclipse onset in the northern hemisphere; then with the eclipse onset, the southern EIA crest weakened gradually. At the end of the eclipse, the southern EIA crest almost vanished (Figure 9). At the eastern longitudes where the distance between the northern eclipse zone and its conjugate region is shorter than that in the eastern longitudes, the weakening southern EIA crest fell into the 0.25-curve and its TEC intensity reduction (contrast), relative to the northern EIA crest, was larger as compared to that in the western longitudes. The northern EIA appeared to be slightly enhanced in the local afternoon during the eclipse time period.

Variations in this southern EIA crest were significant and they were accompanied by the development of eclipse-induced conjugate depletion in dTEC, extending equatorward into the polarward vicinity of the crest, and therefore their direct impacts on the ionosphere adjacent to the conjugate depletion can be important. These EIA variations will be discussed further in the next Section.

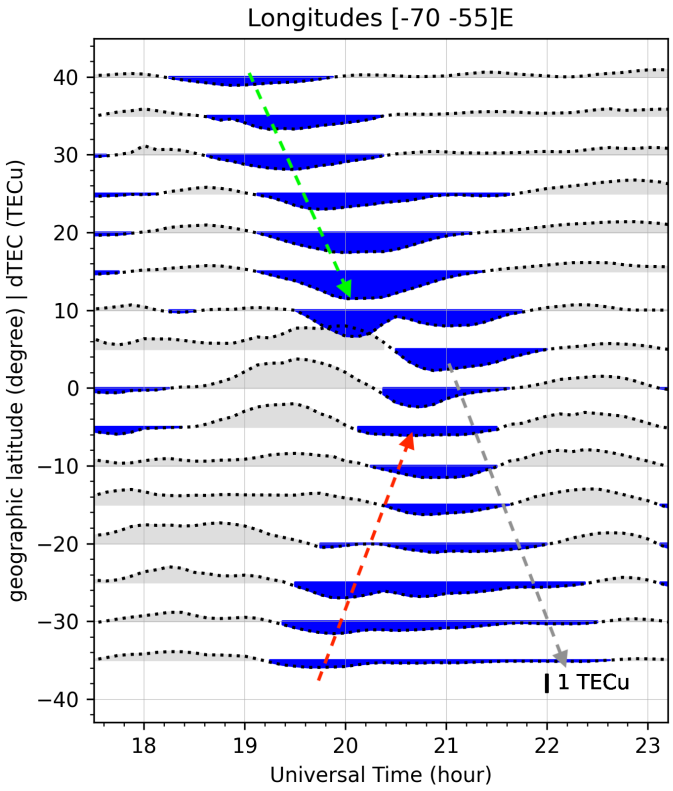


Figure 7: UT time variation of dTEC (in TECu) derived using the 120-min sliding window de-trending at geographic latitudes between -35 – 40°N for longitudinal sectors -70 – -55°E. These dTEC values are running averages over ±3.75 min and ±5° to represent characteristic dTEC variations shown in Figure 6. Negative dTEC values are marked as blue shadows.The green arrow represents the disturbance propagation under direct influences of the Moon mask, the green arrow represents equatorward progression of ionospheric disturbances in the conjugate hemisphere during the eclipse time period, and the gray arrow is post-eclipse ionospheric disturbance propagation into the conjugate hemisphere.

## 4 Discussion

Results presented in the prior section reveal a strong correlation between the solar eclipse and ionospheric response in the southern hemisphere. In particular, the southern hemisphere TEC depletion occurred in a region that was conjugate to the eclipse region at the correct time although the conjugate properties vary with latitude, and effects also evolved equatorward as the Moon shadow moved equatorward. We now discuss sever factors that may cause this conjugate ionospheric depletion effect.

### 4.1 Conjugate electric field and electron temperature

Eclipse effects simulations shown in Huba and Drob (2017) indicated a TEC depletion band at 18:30 UT located at -30°N and also equatorward in the South Pacific Ocean, to the west of South America (Figure 6 in Huba and Drob (2017)). At this time,

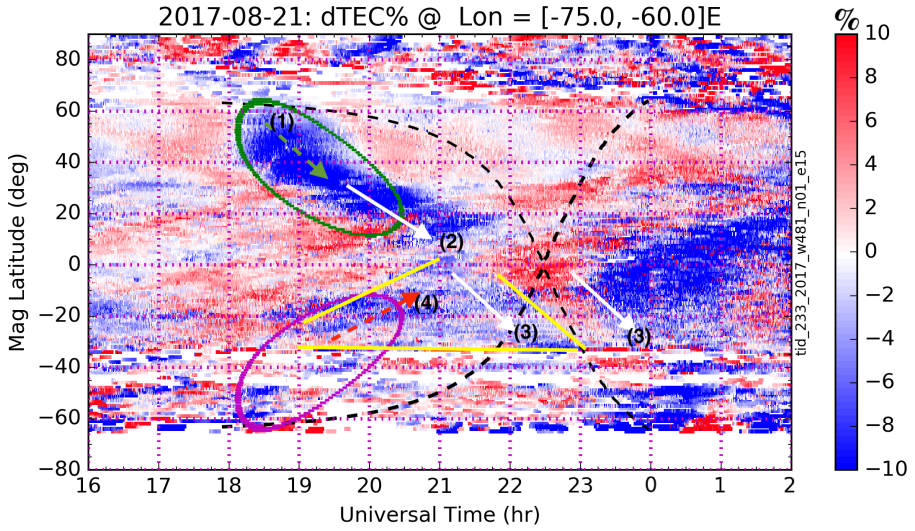


Figure 8: UT vs magnetic latitude variations of dTEC derived using the 120-min sliding window de-trending for longitudinal sectors -75 – -60°E. The southern hemisphere ionospheric effects are identified primarily in a triangle region formed by the three two yellow lines (top). The 0.25 eclipse magnitude is marked by the green line and its conjugate location is marked by the purple line. The green arrow represents the progression direction of density depletion in the eclipse zone, and the white arrow is the eclipse-induced ionospheric wave propagation. Thick dashed line represents the sunset times, and the thin dashed line is the sunset times for corresponding conjugate locations

the conjugate latitudes of the 25% eclipse iso-magnitude circle occurred further in the south, completely beyond this -30°N latitude. Comparison indicates therefore that the predicted depletion reported by Huba and Drob (2017) is not likely to be the same depletion we report here. Instead, modeling results showed an **enhancement** zone, southward of the -30°N depletion and likely conjugate to the northern eclipse. For Huba and Drob (2017), the conjugate electron density enhancement was explained in terms of an enhanced electrostatic field due to reduced conductivity in the eclipse zone (and the simulated density depletion in the non-conjugate region was explained in terms of electric field modification). In particular, enhanced electric field in the conjugate hemisphere would increase the vertically upward component of $\mathbf{E}\times\mathbf{B}$ drift, raising the altitude of the F2-layer and subsequently enhancing TEC through reduced chemical loss by charged exchange and recombination reactions. This mechanism, however, is not applicable to the TEC depletion in our observation.

In the Huba and Drob (2017) simulation, changes in neutral winds, temperature, and composition were not considered. Dang, Lei, Wang, Zhang, et al. (2018)'s separate study provides self-consistent thermosphere-ionosphere coupling during the 2017 eclipse with electrodynamics (but without interhemispheric coupling for mass and thermal exchanges especially at low and mid- latitudes) using the TIEGCM model. In that study, the largest upward vertical component of $\mathbf{E}\times\mathbf{B}$ drift in this simulation appeared to the south of the eclipse conjugate area. However, within the conjugate area, this simulated vertical component remained fairly small and would therefore presumably had little overall effect.

Another TIEGCM-based data assimilation study conducted by Chen et al. (2019) yielded a result of enhanced eastward electric fields at equatorial latitudes. These zonal

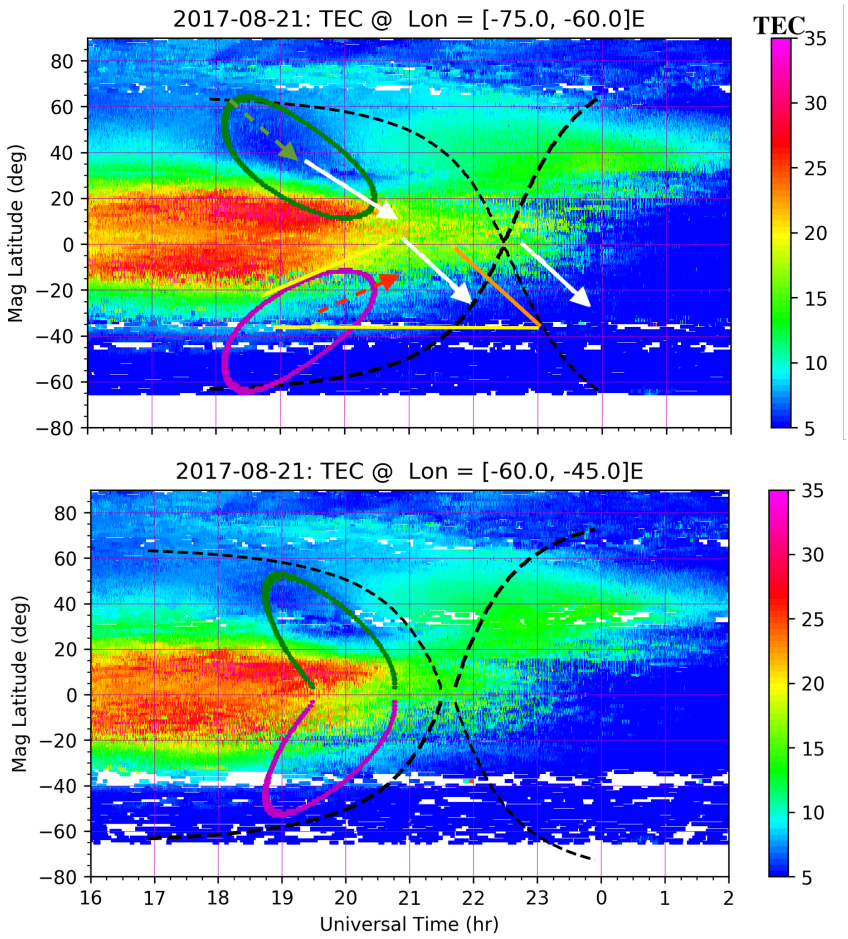


Figure 9: UT vs magnetic latitude variations of TEC for (top) longitudinal sectors -75 – -60°E and (bottom) further west at -60 – -45°E, The arrows and the triangle on the top panel correspond to those in Figure 8.

electric field increases subsequently intensified EIAs, with the enhanced westward electric fields at northern midlatitudes remaining essentially within the Moon shadow due to the dynamo change. Westward electric fields in this configuration can drive downward plasma drift and contribute to electron density depletion in the eclipse zone through increased chemical loss. The westward electric fields of Chen et al. (2019) appeared in the conjugate hemisphere near -20 – -30°N magnetic latitudes, to the south of the southern EIA region, particularly after 20:00 UT. Such a conjugate westward electric field, creating a downward ion drift and potentially contributing to electron density depletion, are indeed qualitatively consistent with our results. However, the magnitude of the westward electric fields was estimated at only $\sim$ 0.1 mV/m translating to a local 2-3 m/s vertical downward drift (i.e., 10 km vertical distance in 1 hour). Furthermore, this electric field timing is problematic for our observations as it occurred 1-hour behind our observed density depletion. Overall, therefore, this conjugate electric field mechanism does not quantitatively fit our depletion observations.

Le et al. (2009); Huba and Drob (2017) simulations also noted significant $T_e$ reduction in both hemispheres, due to reduced photoelectron heating that is conducted along the field line. Such a large $T_e$ reduction would decrease the plasma scale height

in the topside ionosphere, leading to a reduction in TEC. However, Huba and Drob (2017) found that the eclipse induced $T_e$ reduction caused only very small predicted TEC changes ($\leq$ 0.05 TECu). Le et al. (2009)'s simulation, calculated for a different eclipse, showed similar $T_e$ reductions throughout the two hemispheres, but found $N_e$ enhancement in the conjugate ionosphere. We note once again here a strong anti-correlation existed between $N_e$ and $T_e$. In particular, during a reduction in solar EUV irradiation (and thus $N_e$), the associated reduction of photoelectron energy deposition in the upper atmosphere could result in less efficiency for reductions in $T_e$ due to less available electron density to share the total energy input available.

### 4.2 EIA relevance

The southern EIA crest is usually weaker in the afternoon and is asymmetric to the northern one in this season (Luan et al., 2015; Huang et al., 2018). This asymmetric behavior was visible also during the eclipse as described earlier, and therefore the eclipse observation agrees with some of the expected EIA climatology for this season. A major difference from the climatology is that on the eclipse day, the crests were initially (before the eclipse onset) symmetric with similar TEC values (Figure 9), whereas the climatology indicated a consistently weaker southern crest (and an afternoon abatement) during the day. EIA crests are well known for their large day-to-day and diurnal variability. For instance, on 20 August, there was no southern EIA crest in TEC; on 22 August, the southern EIA crest weakening in TEC took place in the afternoon but less dramatically than on 21 August, the eclipse day (Supplement Figure S1). Additionally, dTEC on the 20th and the 22nd also appeared different from values at eclipse time (Supplement Figure SF2), partially due to geomagnetic activity influences as discussed in the next section. Other factors potentially driving EIA variability include lower atmospheric forcing which would modify the equatorial dynamo and thereby affect the EIA fountain effect. These electrodynamic effects, however, would not introduce a substantial asymmetry in EIA crests.

Absent eclipse effects, summer-to-winter trans-equatorial winds (being strong in the afternoon hours) would contribute to a larger northern EIA (with winds uplifting plasma locally) and a weaker southern EIA (with winds pushing down plasma locally). This wind effect was unlikely to be operating prior to the eclipse onset and up to 19 UT, when the EIA crests were actually symmetric. During the eclipse time especially after 19 UT, if these background winds happened to be strong, they would enhance the northern crest and also weaken the southern crest. However, the EIA TEC data do not suggest a clear northern enhancement (e.g., between 19-20 UT) that was comparable to the southern weakening (between 19-20 UT). It is also questionable that the north-to-south trans-equatorial winds could cause the characteristic southern crest weakening that started in its southern (poleward) edge and extended northward (equatorward). However, eclipse presence in the northern hemisphere could create, to the south of the eclipse zone, a perturbed south-to-north (winter-to-summer) pressure gradient. This would create a northward wind component due to atmospheric cooling in the shadow, acting counter to the background trans-equatorial flow. This wind disturbance was observed by (Harding et al., 2018). This mechanism tends to produce an opposite EIA asymmetry, weakening the north EIA crest (by providing a downward ion drift) and enhancing the southern crest. We therefore conclude that the eclipse induced disturbance neutral winds alone were likely not responsible for the observed weakening of the southern EIA.

Electric field disturbances in the local and the conjugate hemispheres at eclipse time would be expected, as discussed in the previous section, but to date simulation results are not quite consistent in producing this feature. Nevertheless, it can be stated that while a westward electric field increase during the Moon shadow passage at mid latitudes appears promising, this effect is not likely to significantly affect the observed dTEC, since

calculated conjugate electric fields are too weak and furthermore the time of their occurrence is too late.

In conclusion, the EIA southern crest weakening was observed during the northern eclipse period whereas the northern crest was much more stable. Although this EIA asymmetry pattern was consistent with some of the established EIA climatology, several known factors that are normally considered as contributing to the substantial day-to-day EIA variability cannot be attributed positively in this eclipse event to this weakening and the associated EIA crest asymmetry on the eclipse day. Accordingly, we argue that other eclipse related processes could have played a role and contributed to EIA variability.

### 4.3 Eclipse induced plasma pressure gradient reduction

Factoring in the discussion above, a new mechanism is proposed here with better consistency with known thermal behavior during eclipses and with observed TEC eclipse time behavior in both hemispheres. It is clear that, in the eclipse region, plasma density (to a large degree), electron temperature, and ion temperature (to a less degree) all drop. For example, Hairston et al. (2018) reported a 500-1000K drop in $T_e$ during this eclipse in DMSP data. The F region $T_e$ in the direct, partial eclipse zone at the mid latitude Millstone Hill incoherent scatter radar experienced a similar temperature drop although with smaller magnitude (Goncharenko et al., 2018). Given these trends, eclipse time plasma pressure (proportional to plasma density and plasma temperature ($T_e$ + $T_i$)) should decrease as well, and this pressure would have a larger reduction amplitude compared to either of its constituent quantities. This pressure drop would lead to a eclipse-induced plasma pressure gradient, oriented downward along the flux tubes at mid- and low latitudes in the eclipse hemisphere, and directed northward at equatorial latitudes (Figure 1, right panel).

The resulting plasma pressure gradient imbalance during the eclipse would facilitate enhanced efficiency in field-aligned plasma flow in various flux tubes affected by the Moon shadow. When the eclipse shadow arrives at lower latitudes where flux tubes have a shorter length (Figure 1, right panel), this field-aligned transport would operate efficiently for those flux tubes that transverse the F2 region topside ionosphere. For instance, the flux tube at the L-shell intersects 20° magnetic latitudes at a 700-800 km apex altitude. However, plasmasphere flux tubes where the field-aligned thermal conduction is strong would experience less this effect, as the conduction would act to smooth out plasma temperature hemispheric differences (Huba & Drob, 2017). As a result, the overall plasma fountain above the magnetic equator F region would be skewed towards the northern eclipse hemisphere (unlike under a normal situation, with diffusion equally northward and southward), and the northern EIA could therefore be maintained or even intensified. This result is inherently asymmetric, since the southern EIA would be weakened due to a lack of sufficient plasma pressure to drive southward diffusion.

It is important to note that this overall eclipse scenario is not analogous to the condition where a long flux tube connects one hemisphere on the dayside to the other one on the nightside via the plasmasphere. In the eclipse scenario here, the equatorial eastward electric field would still create $\mathbf{E}\times\mathbf{B}$ drift that would continuously uplift the fountain plasma, generated by substantial daylight photo-ionization up to high altitudes. The eclipse induced disturbance in neutral winds would also cause a northward ion flow, but this flow would be increasingly weaker away from the eclipse region and hence it would have very limited effects on the southern hemisphere.

### 4.4 Magnetic disturbance effect

Another possibility for generation of the depletion progression we observed lies in whether the effect originated from geomagnetic activity at southern high latitudes. This does not appear likely in the event we studied. In particular, on 20 August, no similar depletion in the aforementioned triangle region nor within the conjugate 0.25-curve region (determined for the eclipse day) was found, although AE indices on both 20 August and 21 August were very similar (Supplement Figure SF2). In fact, the largest disturbances for both days occurred under conditions with AE at ∼750+ nT at ∼ 09UT, with no connection to TEC perturbations after 18 UT. The second largest disturbance occurred very briefly at 18 UT with maximum AE ∼700 nT, but this AE spike produced dayside poleward TIDs only in the northern polar region (Figure 8, a feature similar to what was reported in Zhang, Erickson, et al. (2019). Furthermore, in the southern hemisphere, the depletion in dTEC in the eclipse conjugate region and the triangle region was predominately located at magnetic -30°N latitudes and equatorward, starting prior to 19 UT. Thus, the depletion progression slope was far too small to be consistent with an auroral disturbance source at -60°N at 18 UT, and we therefore judge the AE spike at 18 UT as largely irrelevant to the conjugate depletion. Finally, examining the Hemispheric Power indices at these times for both northern and southern hemispheres shows consistency in key energy input features as represented by AE.

We note that 22 August was more geomagnetically disturbed, and in particular AE was above 500 nT for two hours between 12-14 UT. During this period, southern hemispheric TIDs arrived at the latitudes where the conjugate depletion was identified on the eclipse day as well as higher and lower geomagnetic latitudes (Supplement Figure SF2). It is clear that the magnetic disturbance drove TID symmetry between northern and southern hemispheres. It is therefore clear also that the southern EIA weakening cannot be uniquely tied to eclipse conjugate effects or geomagnetic activity effects. However, the latter effects can indeed be uniquely traced back to its auroral source region.

## 5 Summary

This study investigates ionospheric conjugate perturbations during the 21 August 2017 solar eclipse using ground based GNSS TEC observations. Differential TEC was determined by de-trending the smooth background ionospheric variation within 2-hour long sliding windows. Results for 1-hour long time windows were similar but with smaller amplitudes. Observations identified two categories of conjugate ionospheric perturbations.

The first category was represented by post-eclipse large scale TIDs which traveled into the southern hemisphere approximately in alignment with the Moon-shadow moving direction. These post-eclipse TIDs were consistent with some of the simulated large TADs and the associated electron density disturbances.

The second category was represented by observations of TEC depletion in the southern hemisphere, conjugate to the northern eclipse zone, with at least 25% eclipse magnitude. The depletion occurred at up to 1 TECu less than a 2-hour window background average, or ∼2 TECu (10-15%) less than TEC at the onset of this eclipse effect. This depletion started at higher southern latitudes and continued to be present for 2-3 hours as it moved into lower latitudes at a similar pace as the Moon shadow moved equatorward, with intensification located at ∼ -20°N. Later in the event, this density depletion and the arriving LSTIDs formed an overlapping zone at lower latitudes. Evolution of this conjugate depletion was coincident with a weakening and eventually disappearing southern EIA, with similar timing and plausible effect as southern EIA evolution during the northern eclipse period.

TEC depletion and weakening EIA are features that are not unique to the eclipse day as compared to other days surrounding the event. However, TEC variations observed in the eclipse conjugate hemisphere cannot be fully ascribed to magnetic disturbances nor to other theorized mechanisms previously suggested, including conjugate electric field driven dynamics due to the eclipse induced dynamo change, and plasma thermal contraction presumably throughout both hemispheres due to eclipse induced photoelectron reduction. In particular, enhanced westward electric fields, originating in the Moon shadow region at midlatitudes and magnetically mapping to the conjugate hemisphere, appear initially to be promising drivers of plasma depletion. However, when compared to observations, the previously simulated electric fields were too weak and occurred too late for consistency with data. Other factors that normally contribute to the EIA variability and climatology cannot Instead, we suggest a new eclipse time mechanism associated with a reduced plasma pressure gradient in the flux tube underneath the Moon shadow. As plasma density and plasma temperature (especially electron temperature) both decreased in response to solar irradiation obscuration, an additional plasma pressure gradient was established, directed northward and downward in the northern midlatitudes, and northward at the magnetic equator. Under these conditions, as fountain plasma was pumped continuously upward by the nominal eastward electric field toward higher altitudes, field-aligned diffusion occurred on flux tubes connected to the lower plasma pressure region in the north, but less likely towards the south. Furthermore, a lower neutral pressure gradient in the eclipse region would produce northward disturbance neutral winds predominately in the northern hemisphere low and equatorial latitudes, but not further south in the conjugate hemisphere where they would have moved up the plasma in compensation for skewing of the equatorial plasma fountain toward the other hemisphere. Overall, these eclipse-time processes could contribute to weakening of the southern EIA and ultimately drove the observed conjugate density depletion.

## Acknowledgments

GPS TEC data products and access through the Madrigal distributed data system are provided to the community by the Massachusetts Institute of Technology under support from US National Science Foundation grant AGS-1952737. For eclipse activities, MIT staff members were partially supported by NASA grant NNX17AH71G. SRZ acknowledges the DoD Multidisciplinary Research Program of the University Research Initiative (MURI) project ONR15-FOA-0011. AJC, SRZ and LPG acknowledge the ONR Grant N00014-17-1-2186. Data for TEC processing is provided from the following organizations: UNAVCO, Scripps Orbit and Permanent Array Center, Institut Geographique National, France, International GNSS Service, The Crustal Dynamics Data Information System (CDDIS), National Geodetic Survey, Instituto Brasileiro de Geografia e Estatística, RAMSAC CORS of Instituto Geográfico Nacional de la República Argentina, Arecibo Observatory, Low-Latitude Ionospheric Sensor Network (LISN), Topcon Positioning Systems, Inc., Canadian High Arctic Ionospheric Network, Institute of Geology and Geophysics, Chinese Academy of Sciences, China Meteorology Administration, Centro di Ricerche Sismologiche, Système d'Observation du Niveau des Eaux Littorales (SONEL), RENAG : REseau NAtional GPS permanent, GeoNet - the official source of geological hazard information for New Zealand, GNSS Reference Networks, Finnish Meteorological Institute, and SWEPOS - Sweden. Original TEC data from Madrigal database (`http://cedar.openmadrigal.org/openmadrigal/`) can be found here: `https://w3id.org/cedar?experiment_list=experiments2/2017/gps/21sep17&file_list=gps170921g.002.hdf5` and the line-of-sight TEC which are used for differential calculation is here `https://w3id.org/cedar?experiment_list=experiments2/2017/gps/21sep17&file_list=los_20170921.001.h5`

## References


Astafyeva, E. (2019). Ionospheric Detection of Natural Hazards. *Reviews of Geophysics*, *3*(6), 673.

Azeem, I., Yue, J., Hoffmann, L., Miller, S. D., Straka, W. C., & Crowley, G. (2015). Multisensor profiling of a concentric gravity wave event propagating from the troposphere to the ionosphere. *Geophys. Res. Lett.*, *42*, 7874-7880. doi: 10.1002/2015GL065903

Carlson Jr., H. C. (1966). Ionospheric heating by magnetic conjugate-point photoelectrons. *Journal of Geophysical Research (1896-1977)*, *71*(1), 195-199. Retrieved from `https://agupubs.onlinelibrary.wiley.com/doi/abs/10.1029/JZ071i001p00195` doi: 10.1029/JZ071i001p00195

Chen, C. H., Lin, C.-H. C., & Matsuo, T. (2019). Ionospheric responses to the 21 August 2017 solar eclipse by using data assimilation approach. *Progress in Earth and Planetary Science*, *6*(1), 1–9.

Cherniak, I., & Zakharenkova, I. (2018). Ionospheric total electron content response to the great american solar eclipse of 21 august 2017. *Geophysical Research Letters*, *45*(3), 1199-1208. Retrieved from `https://agupubs.onlinelibrary.wiley.com/doi/abs/10.1002/2017GL075989` doi: 10.1002/2017GL075989

Chou, M.-Y., Lin, C. C. H., Shen, M.-H., Yue, J., Huba, J. D., & Chen, C.-H. (2018). Ionospheric disturbances triggered by spacex falcon heavy. *Geophysical Research Letters*, *45*(13), 6334-6342. Retrieved from `https://agupubs.onlinelibrary.wiley.com/doi/abs/10.1029/2018GL078088` doi: 10.1029/2018GL078088

Cnossen, I., Ridley, A. J., Goncharenko, L. P., & Harding, B. J. (2019). The response of the ionosphere-thermosphere system to the 21 august 2017 solar eclipse. *Journal of Geophysical Research: Space Physics*, *124*(8), 7341-7355. Retrieved from `https://agupubs.onlinelibrary.wiley.com/doi/abs/10.1029/2018JA026402` doi: 10.1029/2018JA026402

Coster, A., Herne, D., Erickson, P., & Oberoi, D. (2012). Using the Murchison Widefield Array to observe midlatitude space weather. *Radio Science*, *47*, RS0K07. doi: 10.1029/2012RS004993

Coster, A. J., Goncharenko, L., Zhang, S.-R., Erickson, P. J., Rideout, W., & Vierinen, J. (2017). GNSS Observations of Ionospheric Variations During the 21 August 2017 Solar Eclipse. *Geophys. Res. Lett.*, *44*, 12. doi: 10.1002/2017GL075774

Dang, T., Lei, J., Wang, W., Burns, A., Zhang, B., & Zhang, S.-R. (2018). Suppression of the polar tongue of ionization during the 21 August 2017 solar eclipse. *Geophyical Research Letters*.

Dang, T., Lei, J., Wang, W., Zhang, B., Burns, A., Le, H., ... Wan, W. (2018). Global Responses of the Coupled Thermosphere and Ionosphere System to the August 2017 Great American Solar Eclipse. *Journal of Geophysical Research: Space Physics*, *123*(8), 7040–7050.

Ding, F., Wan, W., Ning, B., & Wang, M. (2007). Large-scale traveling ionospheric disturbances observed by GPS total electron content during the magnetic storm of 29-30 October 2003. *Journal of Geophysical Research (Space Physics)*, *112*, A06309. doi: 10.1029/2006JA012013

Eisenbeis, J., Occhipinti, G., Astafyeva, E., & Rolland, L. (2019). Short- and long-wavelength tids generated by the great american eclipse of 21 august 2017. *Journal of Geophysical Research: Space Physics*, *124*(11), 9486-9493. Retrieved from `https://agupubs.onlinelibrary.wiley.com/doi/abs/10.1029/2019JA026919` doi: 10.1029/2019JA026919

Evans, J. V., & Gastman, I. J. (1970). Detection of conjugate photoelectrons at millstone hill. *Journal of Geophysical Research (1896-1977)*, *75*(4), 807-815. Retrieved from `https://agupubs.onlinelibrary.wiley.com/doi/abs/`

10.1029/JA075i004p00807 doi: 10.1029/JA075i004p00807

Goncharenko, L. P., Erickson, P. J., Zhang, S.-R., Galkin, I., Coster, A. J., & Jonah, O. F. (2018). Ionospheric Response to the Solar Eclipse of 21 August 2017 in Millstone Hill (42N) Observations. *Geophyical Research Letters*, *45*(10), 4601–4609.

Hairston, M. R., Mrak, S., Coley, W. R., Burrell, A., Holt, B., Perdue, M., ... Power, R. (2018). Topside ionospheric electron temperature observations of the 21 august 2017 eclipse by dmsp spacecraft. *Geophysical Research Letters*, *45*(15), 7242-7247. Retrieved from https://agupubs.onlinelibrary.wiley.com/doi/abs/10.1029/2018GL077381 doi: 10.1029/2018GL077381

Harding, B. J., Drob, D. P., Buriti, R. A., & Makela, J. J. (2018). Nightside detection of a large-scale thermospheric wave generated by a solar eclipse. *Geophysical Research Letters*, *45*(8), 3366-3373. Retrieved from https://agupubs.onlinelibrary.wiley.com/doi/abs/10.1002/2018GL077015 doi: 10.1002/2018GL077015

He, L., Heki, K., & Wu, L. (2018). Three-dimensional and trans-hemispheric changes in ionospheric electron density caused by the great solar eclipse in north america on 21 august 2017. *Geophysical Research Letters*, *45*(20), 10,933-10,940. Retrieved from https://agupubs.onlinelibrary.wiley.com/doi/abs/10.1029/2018GL080365 doi: 10.1029/2018GL080365

Huang, H., Lu, X., Liu, L., Wang, W., & Li, Q. (2018). Transition of interhemispheric asymmetry of equatorial ionization anomaly during solstices. *Journal of Geophysical Research: Space Physics*, *123*(12), 10,283-10,300. Retrieved from https://agupubs.onlinelibrary.wiley.com/doi/abs/10.1029/2018JA026055 doi: 10.1029/2018JA026055

Huba, J. D., & Drob, D. (2017). SAMI3 prediction of the impact of the 21 August 2017 total solar eclipse on the ionosphere/plasmasphere system. *Geophyical Research Letters*, *44*(12), 5928–5935.

Le, H., Liu, L., Yue, X., & Wan, W. (2009). The ionospheric behavior in conjugate hemispheres during the 3 October 2005 solar eclipse. *Annales Geophysicae*, *27*(1), 179–184.

Lei, J., Dang, T., Wang, W., Burns, A., Zhang, B., & Le, H. (2018). Long-Lasting Response of the Global Thermosphere and Ionosphere to the 21 August 2017 Solar Eclipse. *Journal of Geophysical Research: Space Physics*, *123*(5), 4309–4316.

Lin, C. Y., Deng, Y., & Ridley, A. (2018, April). Atmospheric Gravity Waves in the Ionosphere and Thermosphere During the 2017 Solar Eclipse. *Geophyical Research Letters*.

Liu, J. Y., Sun, Y. Y., Kakinami, Y., Chen, C. H., Lin, C. H., & Tsai, H. F. (2011). Bow and stern waves triggered by the Moon's shadow boat. *Geophys. Res. Lett.*, *38*, L17109. doi: 10.1029/2011GL048805

Luan, X., Wang, P., Dou, X., & Liu, Y. C.-M. (2015). Interhemispheric asymmetry of the equatorial ionization anomaly in solstices observed by cosmic during 2007–2012. *Journal of Geophysical Research: Space Physics*, *120*(4), 3059-3073. Retrieved from https://agupubs.onlinelibrary.wiley.com/doi/abs/10.1002/2014JA020820 doi: 10.1002/2014JA020820

Lyons, L. R., Nishimura, Y., Zhang, S.-R., Coster, A. J., Bhatt, A., Kendall, E., & Deng, Y. (2019). Identification of auroral zone activity driving large-scale traveling ionospheric disturbances. *Journal of Geophysical Research: Space Physics*.

MacPherson, B., González, S. A., Sulzer, M. P., Bailey, G. J., Djuth, F., & Rodriguez, P. (2000). Measurements of the topside ionosphere over Arecibo during the total solar eclipse of February 26, 1998. *Journal of Geophysical Research: Space Physics (1978–2012)*, *105*(A10), 23055–23067.

Maurice, J. P. S., Ambili, K. M., & Choudhary, R. K. (2011). Local electrodynam-

ics of a solar eclipse at the magnetic equator in the early afternoon hours. *Geophyical Research Letters*, *38*(4), n/a–n/a.

Mrak, S., Semeter, J., Drob, D., & Huba, J. D. (2018). Direct EUV/X-ray Modulation of the Ionosphere during the August 2017 Total Solar Eclipse. *Geophyical Research Letters*.

Müller-Wodarg, I. C. F., Aylward, A. D., & Lockwood, M. (1998). Effects of a mid-latitude solar eclipse on the thermosphere and ionosphere - A modelling study. *Geophys. Res. Lett.*, *25*, 3787-3790. doi: 10.1029/1998GL900045

Nayak, C., & Yiğit, E. (2018). Gps-tec observation of gravity waves generated in the ionosphere during 21 august 2017 total solar eclipse. *Journal of Geophysical Research: Space Physics*, *123*(1), 725-738. Retrieved from `https://agupubs.onlinelibrary.wiley.com/doi/abs/10.1002/2017JA024845` doi: 10.1002/2017JA024845

Perry, G. W., Watson, C., Howarth, A. D., Themens, D. R., Foss, V., Langley, R. B., & Yau, A. W. (2019). Topside ionospheric disturbances detected using radio occultation measurements during the august 2017 solar eclipse. *Geophysical Research Letters*, *46*(13), 7069-7078. Retrieved from `https://agupubs.onlinelibrary.wiley.com/doi/abs/10.1029/2019GL083195` doi: 10.1029/2019GL083195

Rideout, W., & Coster, A. (2006). Automated GPS processing for global total electron content data. *GPS Solutions*, *10*(3), 219–228.

Rishbeth, H. (1968). Solar Eclipses and Ionospheric Theory. *Space Sci. Rev.*, *8*, 543-554. doi: 10.1007/BF00175006

Saito, A., Fukao, S., & Miyazaki, S. (1998). High resolution mapping of TEC perturbations with the GSI GPS Network over Japan. *Geophys. Res. Lett.*, *25*, 3079-3082. doi: 10.1029/98GL52361

Savitzky, A., & Golay, M. J. E. (1964). Smoothing and differentiation of data by simplified least squares procedures. *Analytical Chemistry*, *36*, 1627-1639.

Sheng, C., Deng, Y., Zhang, S.-R., Nishimura, Y., & Lyons, L. R. (2020). Relative Contributions of Ion Convection and Particle Precipitation to Exciting Large-Scale Traveling Atmospheric and Ionospheric Disturbances. *Journal of Geophysical Research: Space Physics*, *125*(2), 1667.

Shepherd, S. G. (2014). Altitude-adjusted corrected geomagnetic coordinates: Definition and functional approximations. *Journal of Geophysical Research: Space Physics*, *119*(9), 7501-7521. Retrieved from `https://agupubs.onlinelibrary.wiley.com/doi/abs/10.1002/2014JA020264` doi: 10.1002/2014JA020264

Sun, Y.-Y., Liu, J.-Y., Lin, C. C.-H., Lin, C.-Y., Shen, M.-H., Chen, C.-H., ... Chou, M.-Y. (2018). Ionospheric bow wave induced by the moon shadow ship over the continent of united states on 21 august 2017. *Geophysical Research Letters*, *45*(2), 538-544. Retrieved from `https://agupubs.onlinelibrary.wiley.com/doi/abs/10.1002/2017GL075926` doi: 10.1002/2017GL075926

Tsugawa, T., Otsuka, Y., Coster, A. J., & Saito, A. (2007). Medium-scale traveling ionospheric disturbances detected with dense and wide TEC maps over North America. *Geophys. Res. Lett.*, *34*, L22101. doi: 10.1029/2007GL031663

Vierinen, J., Coster, A. J., Rideout, W. C., Erickson, P. J., & Norberg, J. (2016). Statistical framework for estimating GNSS bias. *Atmospheric Measurement Techniques*, *9*, 1303-1312. doi: 10.5194/amt-9-1303-2016

Wang, W., Dang, T., Lei, J., Zhang, S.-R., Zhang, B., & Burns, A. (2019). Physical Processes Driving the Response of the F2-region Ionosphere to the 21 August 2017 Solar Eclipse at Millstone Hill. *Journal of Geophysical Research: Space Physics*.

Wu, C., Ridley, A. J., Goncharenko, L., & Chen, G. (2018). Gitm-data comparisons of the depletion and enhancement during the 2017 solar eclipse. *Geophysical Research Letters*, *45*(8), 3319-3327. Retrieved from `https://agupubs.onlinelibrary.wiley.com/doi/abs/10.1002/2018GL077409` doi:

799 10.1002/2018GL077409
800 Yau, A. W., Foss, V., Howarth, A. D., Perry, G. W., Watson, C., & Huba, J. (2018).
801 Eclipse-Induced Changes to Topside Ion Composition and Field-Aligned Ion
802 Flows in the August 2017 Solar Eclipse: e-POP Observations. *Geophyical*
803 *Research Letters*, *45*(20), 10,829–10,837.
804 Zhang, S.-R., Coster, A. J., Erickson, P. J., Goncharenko, L. P., Rideout, W., &
805 Vierinen, J. (2019). Traveling Ionospheric Disturbances and Ionospheric
806 Perturbations Associated With Solar Flares in September 2017. *Journal of*
807 *Geophysical Research: Space Physics*, *60*(8), 895.
808 Zhang, S.-R., Erickson, P. J., Coster, A. J., Rideout, W., Vierinen, J., Jonah,
809 O., & Goncharenko, L. P. (2019). Subauroral and polar traveling iono-
810 spheric disturbances during the 7-9 September 2017 storms. *Space Weather*,
811 2019SW002325.
812 Zhang, S.-R., Erickson, P. J., Goncharenko, L. P., Coster, A. J., Rideout, W., &
813 Vierinen, J. (2017). Ionospheric Bow Waves and Perturbations Induced by the
814 21 August 2017 Solar Eclipse. *Geophyical Research Letters*, *44*(24), 12,067–
815 12,073.